nature reviews electrical engineering
https://doi.org/10.1038/s44287-024-00117-7

Review article

Check for updates

Nanoscale electromagnetic field imaging by advanced differential phase-contrast STEM

Satoko Toyama [1,2], Takehito Seki [1,2], Yuji Kohno[3], Yoshiki O. Murakami[1], Yuichi Ikuhara[1,4] & Naoya Shibata [1,4,5]

Abstract

Nanoscale electromagnetic fields formed at localized structures such as interfaces play a pivotal role in the properties of state-of-the-art electronic and spintronic devices. Direct characterization of such local electromagnetic fields inside devices is thus crucial for propelling their research and development. In recent years, direct electromagnetic field imaging via differential phase-contrast scanning transmission electron microscopy (DPC STEM) has attracted much attention. Recent developments of tilt-scan averaging systems and magnetic-field-free objective lenses have finally enabled the practical application of this technique to electronic and spintronic devices. This progress has led to the nanoscale, quantitative observations of electric fields of p–n junctions, 2D electron gas and quantum wells, as well as magnetic fields of magnetic domains, magnetic tunnel junctions and antiferromagnets. These studies demonstrate that DPC STEM can observe local electromagnetic fields from nanometre to sub-angstrom length scales across a wide range of materials and devices. In this Review, we describe the basic principles of DPC STEM, discuss its recent developments in both hardware and imaging techniques and finally show its practical applications in device characterization. We emphasize the immense potential of advanced DPC STEM for the research and development of future electronic and spintronic devices.

Sections

Introduction
Theoretical backgrounds of DPC STEM
Recent development of DPC STEM
Material and device applications of advanced DPC STEM
Conclusions and outlook

[1]Institute of Engineering Innovation, School of Engineering, The University of Tokyo, Tokyo, Japan. [2]PRESTO, Japan Science and Technology Agency, Saitama, Japan. [3]JEOL Ltd, Akishima, Tokyo, Japan. [4]Nanostructures Research Laboratory, Japan Fine Ceramics Center, Aichi, Japan. [5]Quantum-Phase Electronics Center (QPEC), The University of Tokyo, Tokyo, Japan. e-mail: shibata@sigma.t.u-tokyo.ac.jp

Key points

- Differential phase-contrast scanning transmission electron microscopy has enabled electromagnetic field imaging at nanometre to sub-angstrom resolution.
- Recent developments in scanning transmission electron microscopy, such as the tilt-scan averaging system and magnetic-field-free lenses, have enabled the practical application of electromagnetic field imaging technique to electronic and spintronic devices.
- Nanoscale and quantitative observations of electric fields in semiconductor devices, including p–n junctions, 2D electron gas and quantum wells, have been achieved.
- Nanoscale magnetic domains, domain walls, switching of magnetization in magnetic tunnel junctions, and atomic antiferromagnetic layers have been visualized.
- Further developments of differential phase contrast, such as in situ biasing and magnetizing technique, will accelerate the research and development of state-of-the-art electronic and spintronic devices.

Introduction

Precise control of nanoscale structures such as interfaces is vital for future electronic and spintronic devices with higher efficiency, increased speed and smaller size. These nanoscale structures strongly correlate with local charge carriers and electromagnetic fields, which determine the properties and performance of the device. Hence, direct characterization of local charge carriers and electromagnetic fields in conjunction with nanoscale structures is essential for the research and development of future electronic and spintronic devices.

Scanning transmission electron microscopy (STEM) is a powerful tool for characterizing materials and devices at subnanometre dimensions. In STEM, a finely focused electron probe is scanned across a sample, capturing the transmitted and scattered electrons at each raster to obtain sample information. Advancements in aberration correctors have enabled the electron beam to be focused down to less than an angstrom[1–5], pushing the resolution of STEM beyond atomic dimensions. Additionally, STEM is distinctive in its versatile imaging modes. A schematic diagram of a typical STEM is shown in Fig. 1a. For atomic structure analysis, we use high-angle annular dark field (HAADF) for imaging heavy elements[6–8] and annular bright field (ABF) for imaging light elements[9–11]. We can obtain local information on elemental distribution and electronic states using energy-dispersive X-ray spectroscopy (EDS)[12] and electron energy loss spectroscopy (EELS)[13,14]. Moreover, recent technological developments in STEM bright-field detectors, such as segmented and pixelated detectors[15–26], have led to the development of new imaging modes. These include atomic structure imaging modes with ultrahigh signal-to-noise ratio for beam-sensitive materials: examples are optimum bright-field imaging[27,28] and electron ptychography[29–31], and the electromagnetic field imaging method using differential phase contrast (DPC)[32–36], which is the focus of this paper. A schematic diagram of DPC STEM is shown in Fig. 1b. DPC STEM detects the deflection of an incident electron beam by the electromagnetic fields of a sample using segmented or pixelated detectors, visualizing the electromagnetic fields at the nanometre or smaller length scale. DPC STEM enables not only high-resolution observations of electromagnetic fields but also simultaneous observation of atomic structures through other STEM imaging modes such as HAADF. An example of DPC STEM observation in a GaAs p–n junction is shown in Fig. 1c–g. In theory, diffusion and combination of electrons and holes at the depletion layer in between n-type and p-type regions induce electric fields pointing from n-type to p-type regions at the equilibrium state. Because the dopant concentrations in p-type and n-type regions are usually small (about 10^{17}–10^{19} atom cm^{-3}), there is almost no structural difference between the two regions. Therefore, almost no contrast appears at the p–n junction when using structure-sensitive imaging such as HAADF (Fig. 1g). DPC STEM clearly visualizes lateral electric fields from n-type to p-type regions, showing the exact position of the p–n junction. Many applications have also shown the usefulness of DPC STEM, such as imaging of electric fields in semiconductors[37–49], polar materials[50–56], atomic electric fields (even within single atoms)[50,57–59] and charge densities[60–65], and imaging of magnetic fields inside magnetic domains, domain walls[66–71] and magnetic skyrmions[72–76].

Recent advances in DPC STEM, particularly the development of tilt-scan-averaged DPC STEM (tDPC STEM)[48,77], have enabled quantitative observations of electromagnetic fields and charge densities in the vicinity of crystalline interfaces such as heterointerfaces and grain boundaries. Another noteworthy development is the magnetic-field-free objective lens[78], which enables high-resolution observation of magnetic materials in a magnetic-field-free environment. These advancements have led to real-space observations of 2D electron gas at wide-gap semiconductor heterointerfaces[79], magnetic domains and walls in polycrystalline magnets, magnetic fields in magnetic tunnel junctions[80] and atomic magnetic fields of an antiferromagnet[81]. Thus, the advanced DPC STEM has the potential to substantially enhance our understanding of device characteristics.

In this Review, we discuss the theoretical background of DPC STEM and recent developments of tDPC STEM and magnetic-field-free objective lenses. Then, we show the application of electromagnetic field observations using the advanced DPC STEM. Finally, we discuss the remaining challenges of electromagnetic field imaging and future directions of this field. Through the discussion, we show how DPC STEM might contribute to the research and development of future nanoscale devices.

Theoretical backgrounds of DPC STEM

In this section, theoretical principles of electromagnetic field imaging by DPC STEM are described. When an electromagnetic field exists perpendicular to the path of an electron, and the electron beam passes through the fields, momentum is transferred to the electrons and their phase will be shifted. The basic concept of DPC STEM is to measure this momentum transfer by splitting the detector on the diffraction plane and taking the subtraction of the intensities detected by the opposing detector segments. The idea of detecting phase information of the incident electron beam by subtracting electron intensities of the opposing detector segments was originally proposed by Rose[32,34]. Dekkers and de Lang substantiated that the differences in the electron intensities of the opposing detector segments correlate with the differential phase of the transmitted electrons, which relates to the electromagnetic fields inside the sample[33]. Waddell and Chapman[82,83]

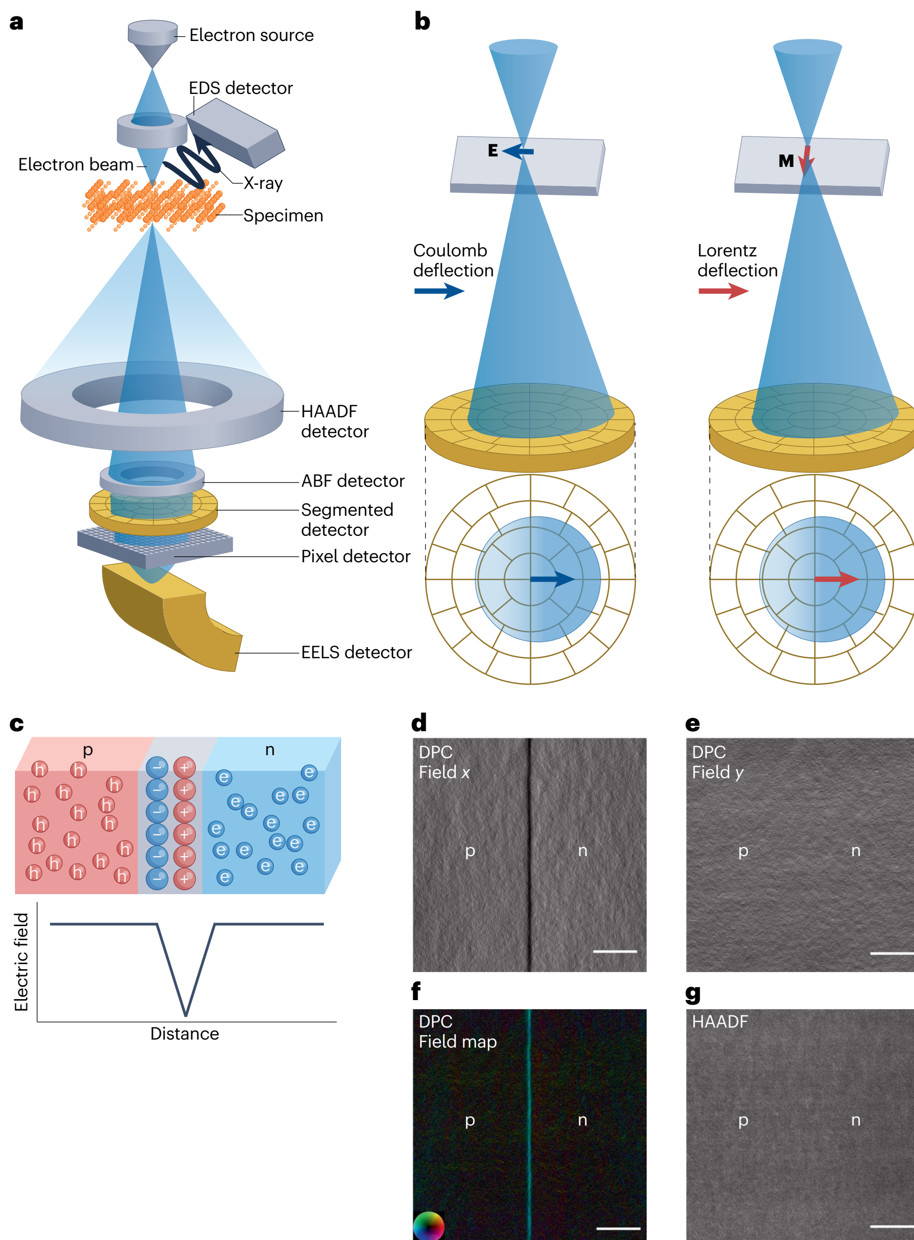

Fig. 1 | Overview of differential phase-contrast scanning transmission electron microscopy techniques. a, Schematic of STEM. The configurations of high-angle annular dark-field (HAADF), annular bright field (ABF), segmented, pixelated, electron energy loss spectroscopy (EELS) and energy-dispersive X-ray spectroscopy (EDS) detectors with respect to the sample are illustrated. **b**, Schematic of differential phase-contrast scanning transmission electron microscopy (DPC STEM) for visualization of electric (left) and magnetic (right) field. When a focused electron probe scans the sample region wherein a leftward electric field or frontward magnetic field exists, the transmitted electrons are deflected to the right. **c**–**g**, The results of p–n junction observation by DPC STEM. **c**, Schematic of p–n junction and its ideal electric field profile. Simultaneously observed images of horizontal (panel **d**) and vertical (panel **e**) components of electric field, colour map of electric field vector (panel **f**) and HAADF STEM images (panel **g**) are shown. In panel **f**, the inset colour wheel indicates how colour and shade denote electric field orientation and strength. All scale bars in panels **d**–**g** correspond to 200 nm.

later elucidated that the measurement of the centre of mass (CoM) of the diffraction pattern directly correlates with the electromagnetic fields inside the sample under the phase object approximation, where the electromagnetic field alters only the phase of the incident electron beam.

Theoretical studies of phase imaging using segmented or pixelated detectors have evolved substantially since these seminal works[57,84–98]. Here, we start with the classical framework of electromagnetic field imaging in DPC STEM, followed by a quantum mechanical framework based on Ehrenfest's theorem[85,92,93,99–101].

For simplicity, let us assume that the electric ($\mathbf{E}$) and magnetics ($\mathbf{B}$) fields on the sample have only components perpendicular to the electron beam's path, $\mathbf{E}_\perp$ and $\mathbf{B}_\perp$, and they are uniform throughout the thickness of the sample. In the classical framework, we can describe the momentum transfer ($\Delta\mathbf{p}_\perp$) to the transmitted electron beam by the electromagnetic fields through the Coulomb and Lorentz forces:

$$\Delta\mathbf{p}_\perp = -\frac{et}{v}\left(\mathbf{E}_\perp(\mathbf{r}) + \mathbf{v}\times\mathbf{B}_\perp(\mathbf{r})\right) \quad (1)$$

In equation (1), e is the electron charge, t is the thickness of the sample, $\mathbf{v}$ is the velocity of the electron and $\mathbf{r}$ is the real-space coordinates of a sample plane (perpendicular to the path of the electron beam). The deflection angle θ can be described using the electron momentum $p_\parallel = h/\lambda$, where h is Plank's constant and λ is the electron's wavelength,

Box 1 | Comparisons of detectors for DPC STEM imaging

The recent rapid development in bright-field detectors for scanning transmission electron microscopy (STEM) has played a crucial role in the progress of differential phase-contrast (DPC) STEM. This Box compares the main features of two types of bright-field detectors for DPC STEM: segmented and pixelated detectors[15,20,21,23–26].

Segmented detectors, which are based on a photomultiplier system[15] or semiconductor system, typically consist of 4–40 segments divided in both radial and azimuthal directions. An example of a 40-segmented detector is illustrated in Fig. 1b. In contrast, pixelated detectors typically use a complementary metal–oxide–semiconductor (CMOS)-based system and consist of hundreds-by-hundreds of square pixels. When STEM uses pixelated detectors, it is frequently described as '4D STEM', as the 2D information on the detector plane is combined with the 2D information on the sample plane.

Theoretically, pixelated detectors offer more quantitative electromagnetic field imaging than segmented detectors, as discussed in the main text. However, for now, segmented detectors often hold practical advantages. Currently, a notable limitation with pixelated detectors is their read-out speed. Recent technological advancements, such as the development of hybrid-array detectors, have realized fast detection speeds (around 10 μs per pixel)[24]. However, segmented detectors still offer much faster detection speed, in the submicrosecond per pixel range. This rapid detection capability is especially advantageous for tilt-scan-averaged DPC (tDPC) STEM and in situ DPC experiments. Because tDPC STEM requires signal detection at each beam-tilt condition, slower detectors result in a very slow frame rate[77]. In situ DPC experiments require fast beam scanning and fast detectors to track changes in the sample over time. Another issue is the computational cost. Pixelated detectors generate vast amounts of data, often reaching hundreds of gigabytes for one image. This data volume can lead to time and financial costs for data transfers and processing.

Given these factors, selection of an appropriate DPC STEM detector should be based on the balance of the following points: quantitativeness, computational cost, tDPC and in situ capabilities. It should be noted that both the speed of pixelated detectors and the quantitativeness of segmented detectors have been improving year by year[25,77,178]. For example, ultrafast event-driven pixelated detectors have been recently developed[179,180]. For each incoming electron on the detector, the point of impact and time of arrival are monitored. When this is combined with the probe position at each time, the 4D STEM dataset can be obtained. This detector can accelerate the detection speed of pixelated detectors up to the submicrosecond regime by skipping the readout of pixels with zero counts. Further developments are expected to mitigate the current limitations of both detectors.

and $\Delta\mathbf{p}_\perp$: $\tan\theta = \Delta p_\perp / p_\parallel$. As the deflection angle is usually sufficiently small, $\tan\theta \approx \theta$, θ can be described by using equation (1) as:

$$\theta = -\frac{e\lambda t}{hv}(\mathbf{E}_\perp(\mathbf{r}) + \mathbf{v}\times\mathbf{B}_\perp(\mathbf{r})) \qquad (2)$$

In this model, the deflection of transmitted electrons can be seen as the simple shift of the bright-field disc of the incident electron beam. This model is therefore sometimes referred to as the 'rigid shift model'. In this model, the deflection angle θ can be measured by subtracting electron intensities of the opposing detector segments relative to the optical axis.

Although this rigid shift model is valid in situations where the electromagnetic fields are uniform within the electron probe size, for example measuring uniform magnetic fields inside magnetic domains, it is too simplistic for situations where the electromagnetic field varies within the electron probe size, for example observing inside the magnetic domain walls. In these cases, the rigid shift model breaks down, and the quantum mechanical framework should be considered.

Ehrenfest's theorem can be used for including a quantum mechanical framework in equation (2). According to this theorem, the expectation value of the quantum operator for particle momentum should behave like the momentum of the classical particle Therefore, in equation (2), the deflection angle θ and the electromagnetic fields $\mathbf{E}_\perp$ and $\mathbf{B}_\perp$ can be replaced by their expectation values $\langle\theta\rangle$, $\langle E_\perp\rangle$ and $\langle B_\perp\rangle$, making the equation generally valid. When defining the reciprocal-space coordinates of a plane perpendicular to the electron beam path as $\mathbf{k}$, the expectation values become $\langle\theta\rangle = \lambda\langle k\rangle = \lambda\int\psi^*(\mathbf{k},\mathbf{R})\mathbf{k}\psi(\mathbf{k},\mathbf{R})d\mathbf{k}$, $\langle E_\perp\rangle = \int\psi^*(\mathbf{r},\mathbf{R})\mathbf{E}_\perp(\mathbf{r})\psi(\mathbf{r},\mathbf{R})d\mathbf{r}$, $\langle B_\perp\rangle = \int\psi^*(\mathbf{r},\mathbf{R})\mathbf{B}_\perp(\mathbf{r})\psi(\mathbf{r},\mathbf{R})d\mathbf{r}$. Here, $\psi(\mathbf{k},\mathbf{R})$ and $\psi(\mathbf{r},\mathbf{R})$ represent the electron wavefunctions on the detector and the sample plane, respectively, when the electron probe is positioned at $\mathbf{r} = \mathbf{R}$. Using the electron probability densities on the detector plane, $|\psi(\mathbf{k},\mathbf{R})|^2 = I_{\mathrm{diff}}(\mathbf{k},\mathbf{R})$, and on the sample plane, $|\psi(\mathbf{r},\mathbf{R})|^2 = I_{\mathrm{probe}}(\mathbf{r},\mathbf{R})$, equation (2) can be reformed as:

$$\int \mathbf{k} I_{\mathrm{diff}}(\mathbf{k},\mathbf{R})d\mathbf{k} = -\frac{et}{hv}\int(\mathbf{E}_\perp(\mathbf{r}) + \mathbf{v}\times\mathbf{B}_\perp(\mathbf{r}))I_{\mathrm{probe}}(\mathbf{r},\mathbf{R})d\mathbf{r} \qquad (3)$$

The right side of equation (3) can be simplified when assuming that the electron probe is not altered during the probe scan. The integral over the sample plane on the right side of equation (3) can be rewritten as a convolution with the probe intensity function: $-\frac{et}{hv}(\mathbf{E}_\perp(\mathbf{R}) + \mathbf{v}\times\mathbf{B}_\perp(\mathbf{R}))\otimes I_{\mathrm{probe}}$.

The left side of equation (3) represents the integral of the electron diffraction pattern, weighted by its position on the detector plane. This can be measured by calculating the CoM of the electron diffraction pattern. In an ideal pixelated detector with an infinite number of pixels, accurate CoM measurements can be made. As for a finite detector like a segmented detector, it is possible to measure an approximate CoM, where the intensity is weighted by the geometric centre of mass of each segment[85]. In this case, it is equivalent to approximating that the intensity within each segment is constant. Recently, multisegment detectors (such as 40-segment detectors) have been developed. Such detectors are practically useful because they allow fast scanning while maintaining CoM quantitation accuracy[81]. The comparison between pixelated and segmented detectors is discussed in Box 1.

Finally, when defining the measured CoM as DPC signal $\mathbf{S}_{\mathrm{DPC}}(\mathbf{R})$, we obtain

$$\mathbf{S}_{\mathrm{DPC}}(\mathbf{R}) \simeq \frac{et}{hv}(\mathbf{E}_\perp(\mathbf{R}) + \mathbf{v}\times\mathbf{B}_\perp(\mathbf{R}))\otimes I_{\mathrm{probe}} \qquad (4)$$

Equation (4) shows that the measured CoM at the position **R** has linear correlation with the electric field and the cross-product of electron velocity and magnetic field at **R**, all convoluted with the electron-probe point spread function within the phase object approximation. Sample thickness t can be estimated by EELS[102,103] or convergent beam electron diffraction technique[104]. Thus, DPC STEM can quantitatively visualize electromagnetic fields inside the sample.

It should be noted that the range where the phase object approximation remains valid is not straightforward. When an atomically sharp probe is used, the phase object approximation can break down for several nanometres of sample thickness, owing to the dynamical effects associated with the strong atomic potential[85]. However, when using a nanometre-sized probe, the situation is different. The strong atomic potential is averaged out inside the nanometre-sized probe, resulting in an almost uniform potential that does not significantly contribute to the DPC signal. Therefore, only mesoscopic phase shifts, which are generally much smaller than the atomic potential, contribute to the DPC signal, making the applicable domain of the phase object approximation wider than an atomically sharp probe. For a p–n junction with dopant density of 10^{19} atom cm^{-3} and a semiconvergent angle of 1 mrad, the phase object approximation remains valid for thicknesses of several hundred nanometres[96]. Thus, it is important to choose the appropriate convergence angle depending on the strength of the electromagnetic field being observed. In cases where the phase object approximation breaks down, the specimen potential might be reconstructed through an iterative algorithm using multislice simulation, as demonstrated in ref. 105. Additionally, it is worth noting that the atomic potential might still contribute to the DPC signal via dynamical diffraction, even when using a nanometre-sized probe, a phenomenon known as diffraction contrast. The phase object approximation can only be adopted when this diffraction contrast is absent or sufficiently weak. Non-ideal situations, such as existing diffraction contrast, defocus or plasmon scattering, in which equation (4) does not work well, have been discussed in detail elsewhere[45,96,106,107].

Recent development of DPC STEM

Tilt-scan-averaged DPC STEM

In this section, we describe the development of tDPC STEM. As mentioned in the Introduction, precisely characterizing the behaviours of electromagnetic fields and carriers associated with interface structures is crucial for understanding the properties of nanoscale devices. Indeed, TEM or STEM allows for high spatial resolution cross-sectional observation of interfaces, but substantial barriers, especially the problem of diffraction contrast, remain in electromagnetic field imaging using Lorentz TEM, electron holography, 4D STEM and DPC STEM[42,44,108,109]. The comparison between electron holography and DPC STEM is discussed in Box 2. The principles of DPC STEM described in the previous section assumed an ideal situation without strong dynamical effects, but in practice, electrons transmitted through crystalline samples are strongly affected by the changes of diffraction conditions with multiple scattering. Moreover, this diffraction effect is highly sensitive to sample bending or other factors such as strain and sample thickness[108]. Therefore, if such factors exist within the specimens, the true CoM changes generated by specimen electromagnetic fields are largely disturbed, and diffraction contrast is superposed on DPC images. Because strains are commonly formed at crystalline interfaces, diffraction contrast often appears as strong signals in DPC images. Therefore, previous studies have often used a technique of arbitrarily tilting the samples about 10° away from the zone axis orientation to circumvent the strong excitation of Bragg reflections[37,96]. However, this sample tilt sometimes worsens the spatial resolution at the crystalline interfaces. This is because the interfaces are inevitably tilted from the exact edge-on condition.

So far, several studies have been reported to overcome this problem. Some studies have introduced a 4D STEM approach that uses edge detection of a bright-field disc by a pixelated detector[110,111]. The edge detection method reduces diffraction contrast by discarding the intensity distribution inside the bright-field disc and measures the rigid shift of the disc to quantify the electromagnetic fields. As discussed in the previous section, a rigid shift model assumes that the electromagnetic field is constant across the electron probe. This technique cannot be applied to cases in which the uniformity of electromagnetic fields cannot be assumed. To overcome such limitations, the sample tilt averaging method has been proposed[41,108,112]. This technique acquires multiple DPC signals by slightly changing the tilt angles of the specimen. To a good approximation, when the sample tilt angle is sufficiently small, the electron beam deflection due to the electromagnetic field is insensitive to the sample tilt. Furthermore, the diffraction contrast can be sensitively changed by the small sample tilt. Therefore, by averaging many DPC images obtained with various different sample tilt angles,

Box 2 | Comparison between DPC STEM imaging and electron holography

Both electron holography and differential phase-contrast scanning transmission electron microscopy (DPC STEM) are techniques that measure the phase shift of transmitted electrons to characterize electromagnetic potentials and fields[42]. In electron holography, biprisms are introduced before the specimen in a specialized transmission electron microscope, which separates the electrons into an object wave and a reference wave. By interfering the object wave with the reference wave, a hologram is formed, allowing quantitative, absolute potential measurements. Electron holography has been applied to various materials, including magnets, thin film devices and nanoparticles[157,177,180–183]. This Box briefly compares the DPC STEM and electron holography techniques.

One major difference is that DPC STEM can be relatively easily performed by introducing a segmented detector into normal STEM, without the need for the specialized transmission electron microscope instrument. Therefore, DPC STEM allows the simultaneous acquisition of structural information through other STEM techniques, such as high-angle annular dark-field imaging and energy-dispersive X-ray spectroscopy analysis. This enables a correlative understanding of atomic structure, chemistry and electromagnetic fields, which is particularly useful for studying crystal defects and heterointerfaces.

Another difference is that DPC STEM primarily measures the electromagnetic field, whereas electron holography measures potential. Although electromagnetic fields and potentials are theoretically interrelated, differentiation or integration image processing can be practically challenging, owing to the increased high-frequency or low-frequency noise[79]. Consequently, DPC STEM should be more advantageous for observing field or charge distributions along with atomic structures, whereas electron holography excels in quantitative measurements of potential distributions.

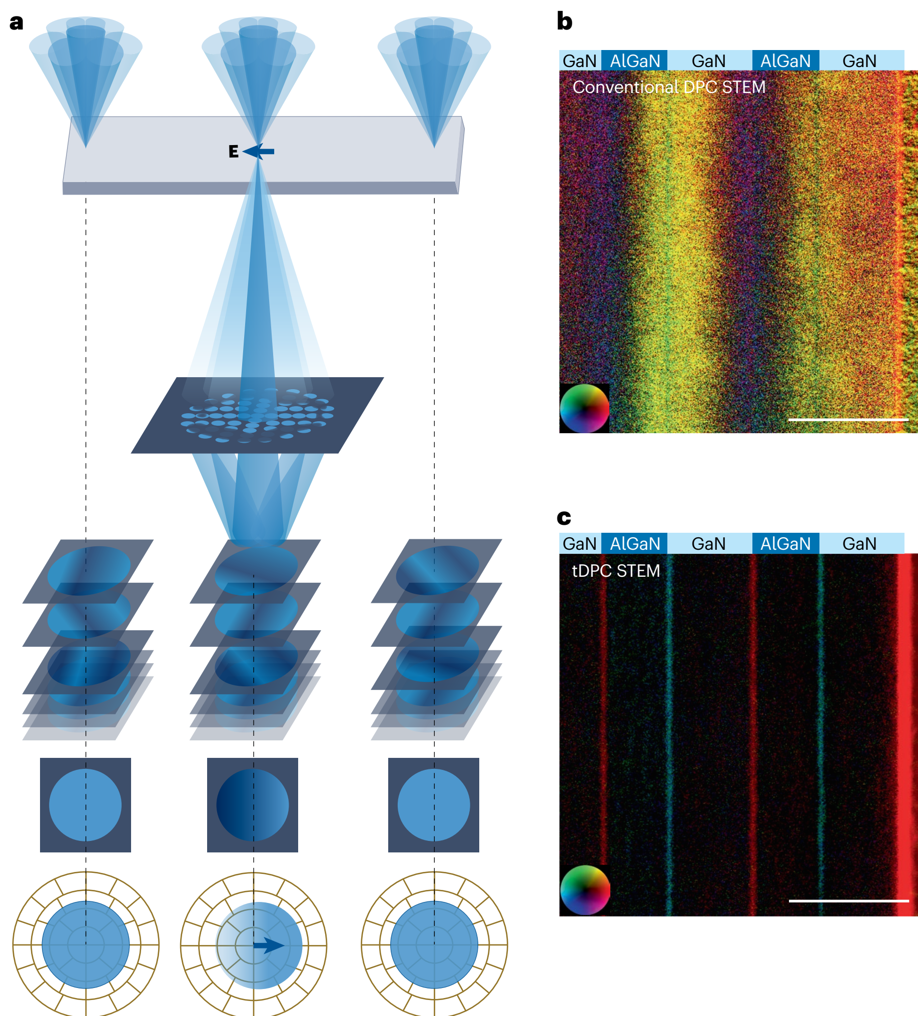

Fig. 2 | Overview of tilt-scan-averaged DPC STEM. **a**, Schematic of tilt-scan-averaged differential phase-contrast scanning transmission electron microscopy (tDPC STEM) technique. The intensity distribution in a bright-field disc originated from diffraction effect can be minimized by averaging multiple beam-tilt condition bright-field discs. Using this averaged bright-field disc, tDPC STEM images are acquired. **b**,**c**, Conventional DPC (panel **b**) and tDPC (panel **c**) images of the same GaN/$Al_{0.14}Ga_{0.86}N$/GaN/$Al_{0.14}Ga_{0.86}N$/GaN heterostructures. The film configurations are shown at the top of the images. In panels **b** and **c**, the inset colour wheel indicates how colour and shade denote electric field orientation and strength. The scale bars in panels **b** and **c** correspond to 30 nm. Panels **b** and **c** adapted with permission from ref. 48.

diffraction contrast can be effectively cancelled out, whereas the true electromagnetic field signals are reinforced. Previous work showed that the diffraction contrasts due to sample bending in a p–n junction sample can be effectively reduced by sample tilt averaging[108]. Those authors also simulated tilt-averaged electron diffraction patterns with Bloch-wave method and quantitatively evaluated the residual diffraction contrast after averaging. Another study proposed a method to evaluate the residual diffraction contrast in the sample-tilt-averaged DPC images by statistical analysis of individual sample-tilted DPC images before averaging[69].

Although the sample tilt-averaging method has been shown to be effective for suppressing diffraction contrast in DPC images, it relies on mechanical sample-tilting systems that include notable errors in tilt angles. In addition, post-image processing for averaging many DPC images might lead to degradation of image resolution. Moreover, substantial electron doses on the sample, which are required for acquiring multiple sample-tilt DPC images from the same sample position, can result in severe electron beam damages. To address these issues, a new beam-tilt-scanning system has been developed[77]. A schematic diagram of tDPC STEM is shown in Fig. 2a. The new scanning system can control the electron beam tilt with respect to the sample while scanning the beam across the sample. This scan system enables the rapid acquisition of the beam-tilt-averaged DPC images. Because there are no mechanical tilt errors, precise and reproducible beam-tilt-averaged DPC images can be acquired. The effectiveness of tDPC STEM was first demonstrated by observing GaN/$Al_{0.14}Ga_{0.86}N$ multi-heterostructures[48]. Such heterostructures are intrinsically strained owing to the lattice mismatch between GaN and $Al_{0.14}Ga_{0.86}N$ layers. Conventional DPC STEM observation shows strong contrast fluctuation within each layer due to the unavoidable diffraction contrast (Fig. 2b). In contrast, tDPC STEM image exhibits almost uniform contrast within each layer, and the interface electric fields, resulting from the mean inner potential difference between GaN and $Al_{0.14}Ga_{0.86}N$ layers, are distinctly visualized (Fig. 2c). The precise beam-tilt control allows us to quantitatively evaluate the residual diffraction contrast in tDPC STEM image by simulating beam-tilt-averaged electron diffraction pattern[113]. These results showed that the diffraction contrast can be substantially reduced in the tDPC STEM image, to about one-twentieth of that in the conventional DPC STEM.

Magnetic-field-free objective lens for magnetic field imaging

In this section, we introduce the development of a magnetic-field-free objective lens that facilitates ultrahigh-resolution magnetic

field imaging of magnetic materials and devices. Spintronic devices require precise control of magnetic structures with length scales of a nanometre or less, which show strong interactions with atomic-scale local structures such as grain boundaries and heterointerfaces. Therefore, it is important to probe local magnetic structures in conjunction with atomic structures simultaneously. However, achieving ultrahigh-resolution magnetic field imaging has been extremely challenging in electron microscopy for many years.

In a high-resolution objective lens, a strong magnetic field is generated in the pole piece, which is used to focus highly accelerated electrons. The sample is placed in between the upper and lower pole pieces, being exposed to almost maximum magnetic field within the pole piece (Fig. 3a). A strong external magnetic field of about 2–3 T is therefore inevitably applied to the sample during observation. When observing magnetic materials, the magnetic structure of the sample, or even the sample itself, has often been altered or even destroyed by the fields. Therefore, a mode with the objective lens off, known as ‘Lorentz mode’, has often been used for observing magnetic materials via electron microscopy[114–117]. However, this mode markedly restricts the spatial resolution, typically to only a few nanometres or so. Consequently, visualizing magnetic materials at high spatial resolution has been an exceedingly challenging task in electron microscopy.

To overcome this limitation, a magnetic-field-free objective lens has been developed[78]. A schematic diagram of this lens is shown in Fig. 3b. The front and back pole pieces are precisely aligned in a mirror-symmetrical arrangement relative to the sample position[118]. The front and back pole pieces apply magnetic fields in opposite directions above and below the sample, thereby effectively cancelling out the magnetic fields at the sample position. In this configuration, we can place strong magnetic fields required for forming atomically sharp electron probe as close to the sample as possible, while keeping the samples in a magnetic-field-free condition.

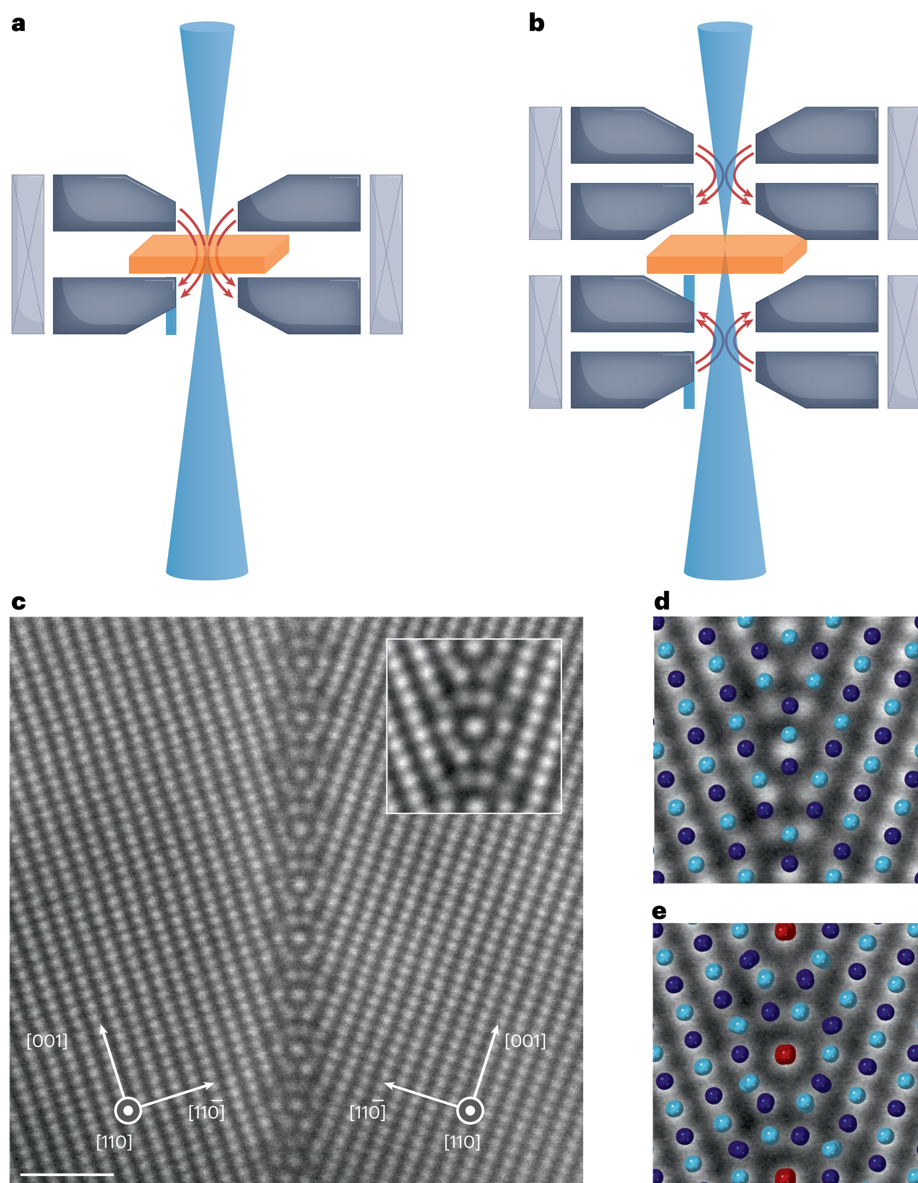

Fig. 3 | Overview of magnetic-field-free objective lenses and its application result. Schematics of conventional (panel **a**) and magnetic-field-free (panel **b**) atomic-resolution objective lenses with respect to the sample. In the conventional objective lenses, a sample (orange rectangle) is placed in between the upper and lower pole pieces, resulting in maximum perpendicular magnetic fields (red arrows) at the sample position. In the magnetic-field-free objective lens, the front and back objective lenses are aligned in exactly mirror-symmetrical configuration with respect to the sample. Because the magnetic fields in these lenses are in opposite directions, this configuration can cancel out the lens magnetic field at the sample plane. High-angle annular dark-field (HAADF) scanning transmission electron microscopy (STEM) images (panel **c**) of a Σ9 symmetrical tilt grain boundary of silicon steel (Fe–3 wt% Si), obtained using the magnetic-field-free objective lens. The inset is the averaged image of the grain boundary structure units. The scale bar corresponds to 1 nm. **d**,**e**, The grain boundary structure units superimposed with the previously predicted and newly discovered structure models, respectively. Panels **c**–**e** adapted from ref. 119.

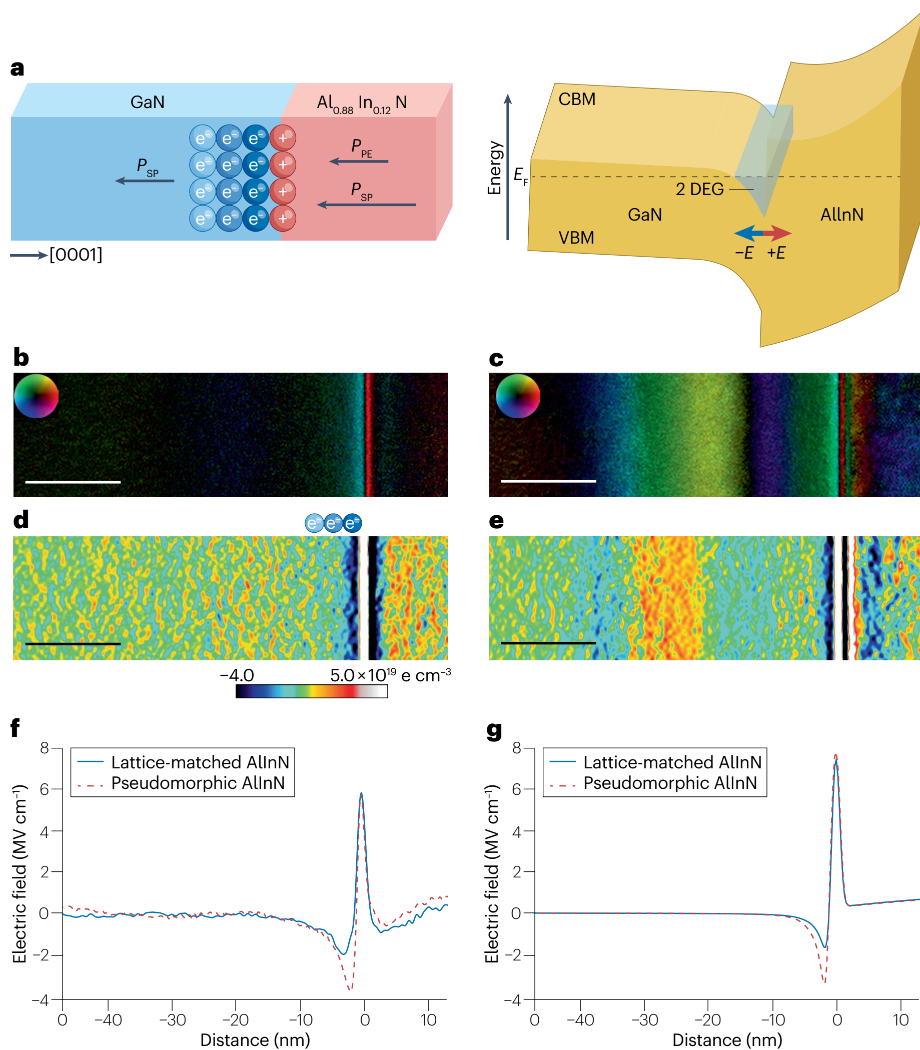

Fig. 4 | Two-dimensional electron gas imaging. **a**, Schematics of the GaN/$Al_{0.88}In_{0.12}N$ heterointerface with the positive polarization-bound charge and 2D electron gas due to the difference in spontaneous polarization (P_{SP}) and piezoelectric polarization (P_{PE}). **b**,**c**, Electric-field-vector colour maps of GaN/$Al_{0.88}In_{0.12}N$ (pseudomorphic AlInN) by tilt-scan-averaged differential phase-contrast scanning transmission electron microscopy (tDPC STEM) (panel **b**) and conventional DPC STEM (panel **c**). The inset colour wheel indicates how colour and shade denote electric field orientation and strength. **d**,**e**, Charge density maps generated by calculating the divergence of the electric-field-vector maps (panels **c** and **d**). All the scale bars in panels **b**–**e** correspond to 20 nm. **f**,**g**, Experimental and simulated horizontal electric field profiles of GaN/$Al_{0.88}In_{0.12}N$ (pseudomorphic AlInN; red dashed line) and GaN/$Al_{0.81}In_{0.19}N$ (lattice-matched AlInN; blue solid line) heterointerfaces. CBM, conduction band minimum; E_F, Fermi energy; VBM, valence band minimum. Panels **a**–**g** adapted from ref. 79.

In combination with state-of-the-art aberration correctors, this lens design allows for atomic-resolution TEM and STEM observations with residual magnetic fields on the samples less than 0.2 mT, far less (under 1/10,000) than those imposed on samples by conventional objective lenses.

An atomic-resolution HAADF STEM image of a Σ9 symmetrical tilt grain boundary of silicon steel (Fe–3 wt% Si) using STEM equipped with the magnetic-field-free objective lens is shown in Fig. 3c–e[119]. Silicon steel, despite being commonly used, poses considerable challenges for atomic structure imaging owing to its soft ferromagnetic nature. However, with this new objective lens, the unique atomic structure of the grain boundary was clearly resolved.

Magnetic-field-free objective lenses are also useful for observing magnetic fields via DPC STEM. This powerful combination allows for unveiling atomic-scale magnetic phenomena that were concealed because of the constraints of conventional high-resolution TEM and STEM. Later, we present several studies that used this lens system with DPC STEM to directly observe local magnetic fields inside magnetic materials and devices.

Material and device applications of advanced DPC STEM

Two-dimensional electron gas imaging

Two-dimensional electron gases (2DEGs) are important components for electronic devices, owing to their highly mobile characteristics[120–122]. Heterointerfaces of GaN-based semiconductors, consisting of AlN, GaN, InN and their compounds, are used in high-electron-mobility transistors, where 2DEGs are spontaneously induced at the interfaces by polarization mismatches[123–125]. The behaviour of 2DEGs within such devices is presumed to be influenced by local atomic-scale defects such as compositional fluctuations, dislocations and unintentional impurities[126,127]. Unfortunately, conventional electrical measurements such as Hall effect measurements[128] measure only overall macroscopic device properties and thus fail to capture such localized information inside devices. Therefore, direct and local observation of 2DEGs is essential for in-depth understanding of mechanisms and properties of these electronic devices.

So far, microscopic characterization of 2DEGs has been attempted by using atomic force microscopy[129,130] and optical laser

probe microscopy[131]. However, these methods are not suitable for cross-sectional observation of 2DEGs formed at heterointerfaces, owing to their sensitivity only to the surface or their limited spatial resolution. Addressing this issue, tDPC STEM was used for directly visualizing 2DEGs formed at GaN-based semiconductor heterointerfaces at subnanometre resolution[79]. Given that substantial strains are typically present at these heterointerfaces, the tilt-scan averaging technique should be particularly advantageous for 2DEG observation. Their study focused on two samples: nearly lattice-matched GaN/$Al_{0.81}In_{0.19}N$ and pseudomorphic GaN/$Al_{0.88}In_{0.12}N$ with lattice mismatches. A schematic diagram of GaN/AlInN polarization mismatches and a band diagram are shown in Fig. 4a. The conventional DPC and tDPC STEM images of the pseudomorphic samples are shown in Fig. 4b,c. The electric field image obtained by conventional DPC STEM shows remarkable contrast fluctuations, not only at the interface but also within each layer. These fluctuations are due to diffraction contrast from the local strain and sample bending within the sample, complicating the extraction of interface charge signals. In contrast, the electric field image obtained by tDPC STEM clearly shows leftward signals (blue contrast) on the GaN side of the heterointerface, indicating the presence of negative charges at the interface. The charge density map (Fig. 4d,e), derived from the divergence of the electric field image, confirms the presence of negative charge at the GaN side of the heterointerface. This distribution of electric field and charge was similarly observed in the lattice-matched sample. Line profiles of the electric field for both samples are shown in Fig. 4f, indicating that the pseudomorphic interface has a stronger negative electric field than the lattice-matched interface. These profiles are consistent with the profiles that are obtained by the Poisson–Schrödinger simulation[132] (Fig. 4g). At the pseudomorphic interface, piezoelectric polarization is induced by tensile strain in addition to the spontaneous polarization. The sum of the two polarizations results in the stronger electric fields at the heterointerface and thus larger amount of 2DEG accumulated.

To extract quantitative sheet charge densities in the two samples, the experimental electric field profiles were fitted with the Fang–Howard wavefunction[133–136]. The results are summarized in Table 1. Experimental quantification of the sheet charge density shows that the amount of 2DEG formed at the pseudomorphic interface is about twice as much as that formed at the lattice-matched interface, consistent with the simulations and previous studies[137,138]. Intriguingly, a positive charge of about 10^{18} atom cm^{-3} was also observed within the AlInN layers. This suggests that the electrons in the 2DEGs are supplied from the AlInN layers to the heterointerface, and the positive charges in the AlInN layer could originate from the donors after supplying the electrons. Previous studies have suggested that unintended donors might be introduced during AlInN film deposition owing to the difference in deposition temperatures between InN and AlN (refs. 137,139,140). The present experimental results indicate that such donors can be the source of 2DEGs formed at the heterointerfaces.

Table 1 | Quantitative sheet charge densities

Method	Lattice-matched-AlInN		Pseudomorphic AlInN	
	2DEG sheet charge (electron cm^{-2})	Ion density in AlInN (electron cm^{-3})	2DEG sheet charge (electron cm^{-2})	Ion density in AlInN (electron cm^{-3})
tDPC experiment	$1.2\pm0.2\times10^{13}$	$5.8\pm0.5\times10^{18}$	$2.6\pm0.3\times10^{13}$	$5.5\pm0.6\times10^{18}$
Simulation	1.9×10^{13}	NA	3.6×10^{13}	NA
Previous studies	$1–3\times10^{13}$ (Hall effect measurement)	$1–3\times10^{18}$ (SIMS)	NA	NA

Summary of quantitative 2D electron gas (2DEG) sheet charge density and ionized donor density in the lattice-matched and pseudomorphic AlInN interface, estimated by tilt-scan-averaged differential phase-contrast (tDPC) scanning transmission electron microscopy images, simulation and previous studies, which use a Hall effect measurement and secondary ion mass spectroscopy (SIMS). NA, not applicable.

Magnetic domain and domain wall imaging in polycrystalline magnets

Polycrystalline permanent magnets are extensively used in a wide range of industrial applications such as motors, generators and sensors[141]. In these magnets, suppressing the nucleation of reversal magnetic domains and pinning the propagation of domain walls by grain boundaries or precipitates are key to control magnetic properties such as coercivity[142–145]. A fundamental understanding of such effects requires simultaneous observation of local magnetic fields and atomic-scale defect structures. However, in polycrystalline materials, the different crystallographic orientation of each grain often leads to pronounced formation of diffraction contrast, which inevitably obscures the extraction of true magnetic field signals from DPC images[69]. Moreover, strong external magnetic fields applied to the sample using conventional

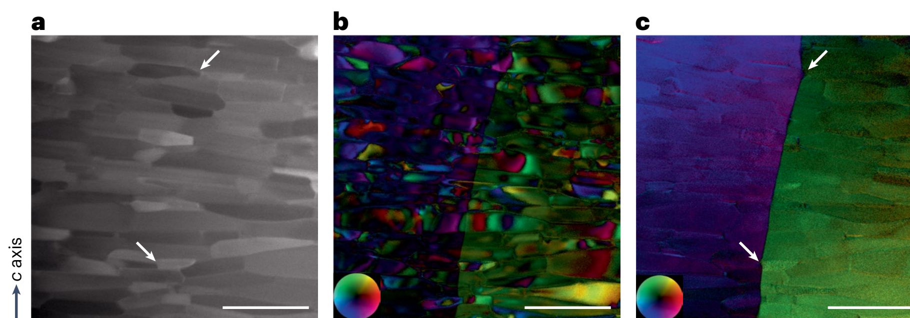

Fig. 5 | Magnetic domain imaging in a polycrystalline magnet. High-angle annular dark-field (panel **a**), conventional differential phase-contrast (DPC) (panel **b**) and tilt-scan-averaged DPC scanning transmission electron microscopy (tDPC STEM) (panel **c**) images of Nd–Fe–B polycrystalline magnet. Panels are obtained from the same sample position. All the scale bars correspond to 500 nm. In panels **b** and **c**, the inset colour wheel indicates how colour and shade denote magnetic field orientation and strength. In panels **a** and **c**, the grain boundaries that are pinning the magnetic domain walls are highlighted by white arrows.

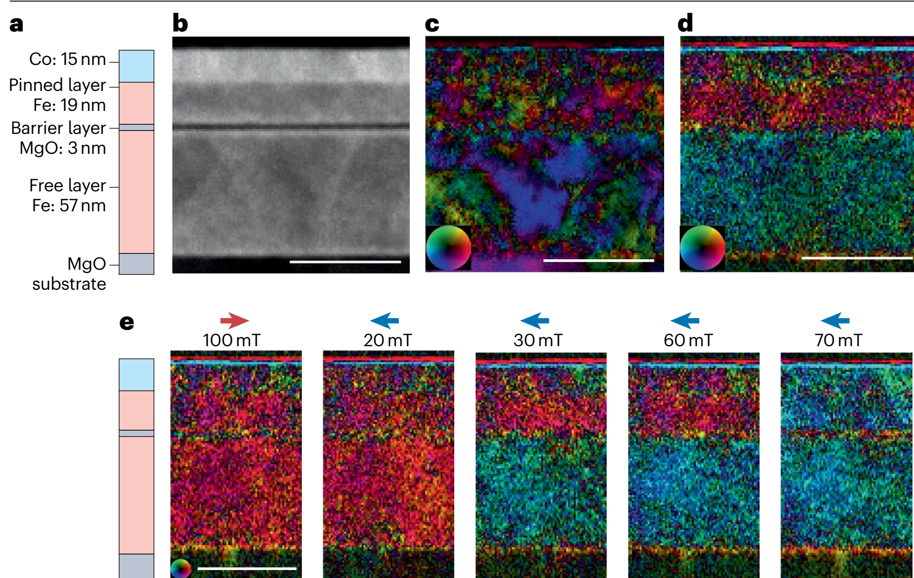

Fig. 6 | Spintronics device imaging. Schematic (panel **a**), high-angle annular dark-field (panel **b**), conventional differential phase-contrast (DPC) (panel **c**) and tilt-scan-averaged DPC scanning transmission electron microscopy (tDPC STEM) (panel **d**) images of a magnetic tunnel junction. **e**, Series of magnetic field images by tDPC STEM of the same sample after applying external magnetic fields. Strength and direction of the external magnetic fields are shown at the top of the images. In panels **c**–**e**, the inset colour wheel indicates how colour and shade denote magnetic field orientation and strength. All scale bars correspond to 50 nm. Adapted with permission from ref. 80.

TEM and STEM lenses can severely alter or even destroy the native magnetic structures of the sample. Thus, the combination of tDPC STEM and magnetic-free-objective lenses should be useful for directly and simultaneously observing local magnetic fields and atomic-scale defect structures in polycrystalline magnets.

A Nd–Fe–B permanent magnet[146,147] was selected as a model sample for visualizing magnetic fields using tDPC STEM and magnetic-field-free objective lens. HAADF STEM, conventional DPC STEM and tDPC STEM images of the Nd–Fe–B polycrystalline sample are shown in Fig. 5a–c. The axis of easy magnetization, the *c* axis, is oriented in the in-plane upward direction of the TEM lamella. The HAADF STEM image (Fig. 5a) reveals the shape of crystal grains by contrast differences. The *c* axes of these grains are well aligned, with a vertical extent of several tens of nanometres and a horizontal extent of approximately 500 nm. In the conventional DPC STEM image (Fig. 5b), there is pronounced contrast attributed to the varying crystal orientations and internal strains within the grains, complicating a detailed analysis of domain wall position. Conversely, the tDPC STEM image (Fig. 5c) effectively minimizes diffraction contrasts, visualizing a 180-degree domain wall separating the downward magnetization on the left side and upward magnetization on the right side. Notably, the domain walls are pinned at specific grain boundaries, as highlighted by the white arrows. Using other analytical STEM techniques such as EDS and EELS, we can also obtain chemical and electronic structure information from such specific grain boundaries directly.

Magnetic field imaging in spintronic devices

In the pursuit of higher-performance computing devices, magnetoresistive random-access memory (MRAM) emerges as a pivotal technology, offering non-volatility, integrability and durability[148,149]. The magnetic tunnel junction (MTJ), comprising two ferromagnetic layers separated by a thin insulating barrier layer, is the key component for MRAM[150–152]. The parallel and antiparallel alignment of magnetization in these two ferromagnetic layers controls the low and high resistivities, respectively, owing to the tunnel magnetoresistance (TMR) effect, retaining binary information. Thus, improving the TMR ratio, which is the relative change in electrical resistance between these two states, is essential for improving MTJ performance[153,154]. The TMR ratio is thought to be influenced by the local atomic structures, especially by the interfaces of the insulator and ferromagnetic layers. Therefore, directly observing the local magnetic fields in the ferromagnetic layers and near their interfaces should provide valuable insights into the TMR properties of MTJs.

For observing magnetic fields inside ferromagnetic layers in MTJs, tDPC STEM with the magnetic-field-free objective lenses was used[80]. As a model sample, the researchers prepared a film on a MgO substrate, consisting of a 57-nm-thick Fe free layer, a 3-nm MgO barrier layer, a 19-nm Fe pinned layer and a 15-nm Co layer to enhance the coercivity of the pinned layer. A schematic illustration of the sample structure and observation results are shown in Fig. 6. In the conventional DPC STEM image (Fig. 6c), it is difficult to distinguish the magnetization directions in the free and pinned Fe layers owing to diffraction contrast caused by the strain and local crystal misorientations. Conversely, the tDPC STEM image (Fig. 6d) clearly visualizes the magnetic fields inside Fe layers: the pinned layer and Co layer show a rightward magnetic field, whereas the free layer shows a leftward magnetic field, identifying the antiparallel state.

To investigate the transition between parallel and antiparallel magnetization states in the MTJ, the researchers applied magnetic fields to the sample ex situ and subsequently observed the sample magnetic fields by tDPC STEM, as shown in Fig. 6e. Initially, on applying a rightward 100-mT external magnetic field in the rightward direction, magnetization of all layers aligned to the right. Subsequently, the researchers increased the leftward external magnetic field step-by-step from 0 mT to 80 mT. When the external field was varied between 20 mT and 30 mT, only the magnetization of the free layer flipped leftward, resulting in the antiparallel state. At an external field between 60 mT and 70 mT, the magnetization of the pinned layer and Co layer also flipped, resulting in the parallel state but in the opposite direction to the initial orientation. This study demonstrated the capability for directly observing the parallel and antiparallel states within the MTJ at nanometre length scale.

Atomic magnetic field imaging of an antiferromagnet

Ultimate understanding of the properties of magnetic devices requires the characterization of magnetic structures down to atomic dimensions. In electron microscopy, atomically resolved magnetic field observation has long been unfeasible, owing to several problems. One problem was the high magnetic field applied to the sample by conventional objective lens, which can disrupt the magnetic structures. This issue was overcome by the development of magnetic-field-free objective lenses[78], as discussed in the previous section. Another problem involves separating atomic electric fields from atomic magnetic fields. Previous studies in non-magnetic materials have indicated that atomic-scale DPC STEM primarily visualizes electric fields emanating from positive atomic nuclei to the surrounding negative electron cloud[58]. Given the relative weakness of the atomic magnetic field signals compared with the atomic electric field signals[155,156], it is necessary to separate the atomic electric field signals from the original DPC signals for visualizing the atomic magnetic field. For materials with macroscopic magnetization, such as ferromagnetic or ferrimagnetic materials, a method in which an external magnetic field is applied to induce magnetization reversal has been proposed. By subtracting the results before and after applying the magnetic field, the magnetic field within the specimen can be extracted[157,158]. However, this magnetization reversal method cannot be applied to antiferromagnetic materials, which do not have macroscopic magnetization.

Observations of antiferromagnetic α-Fe_2O_3 were conducted using atomic-resolution DPC STEM with the magnetic-field-free objective lens[81]. HAADF STEM image with the atomic structure model of α-Fe_2O_3 projected along the [$\bar{1}\bar{1}20$] direction is displayed in Fig. 7a. In the HAADF STEM image, dumbbell-like pairs correspond to the Fe atomic columns within Fe–Fe double atomic layers are present as bright spots. In α-Fe_2O_3, whereas spins at Fe ions in the same Fe–Fe double atomic layers are expected to be ferromagnetically aligned, those in the adjacent Fe–Fe double atomic layers are expected to be antialigned[159]. Within this assumption, the researchers developed a method to cancel out the atomic electric field signals and reinforce the atomic magnetic field signals by image filtering the experimental DPC images. They set up a kernel filter that subtracted the atomic electric field signals from the centre Fe atomic sites, using four neighbouring Fe sites considered to have opposite spin. The signal-to-noise ratio was enhanced by averaging over the crystal units to capture weak atomic magnetic fields. As a result, the magnetic field was successfully observed, and it is estimated to be approximately 0.1% of the electric field signal. The atomic magnetic field and phase-shift image obtained are shown in Fig. 7b,c. In the magnetic-field-vector map, antiparallel contrasts are clearly observed in the adjacent Fe–Fe double atomic layer. These vector map and magnetic phase-shift images are consistent with image simulations that took into account the antiferromagnetic spin orientation measured by neutron scattering[160].

The spin orientation of α-Fe_2O_3 is known to be rotated below 260 K, which is called the Morin transition[161]. Hence, the researchers compared the magnetic DPC image of α-Fe_2O_3 at room temperature with that at about 113 K. The low-temperature DPC images are shown in Fig. 7d–f. Note that images in Fig. 7a–c and d–f were obtained from almost the same sample region. The magnetic vector colour map and corresponding magnetic phase-shift image at low temperature show substantial changes from those obtained at room temperature, consistent with simulated images assuming spin orientation parallel to the [0001] direction below Morin temperature. These results demonstrate that atomic magnetic fields can be imaged in real space and are sensitive to the rotation of spins in antiferromagnets.

Conclusions and outlook

DPC STEM has evolved considerably, owing to the development of better aberration correctors, better detectors, a new tilt-scan system and the magnetic-field-free objective lens. These advancements position DPC STEM as a pivotal tool for characterizing materials and devices at nanometre or even smaller length scales. We thus conclude that the advanced DPC STEM has finally become usable for characterizing

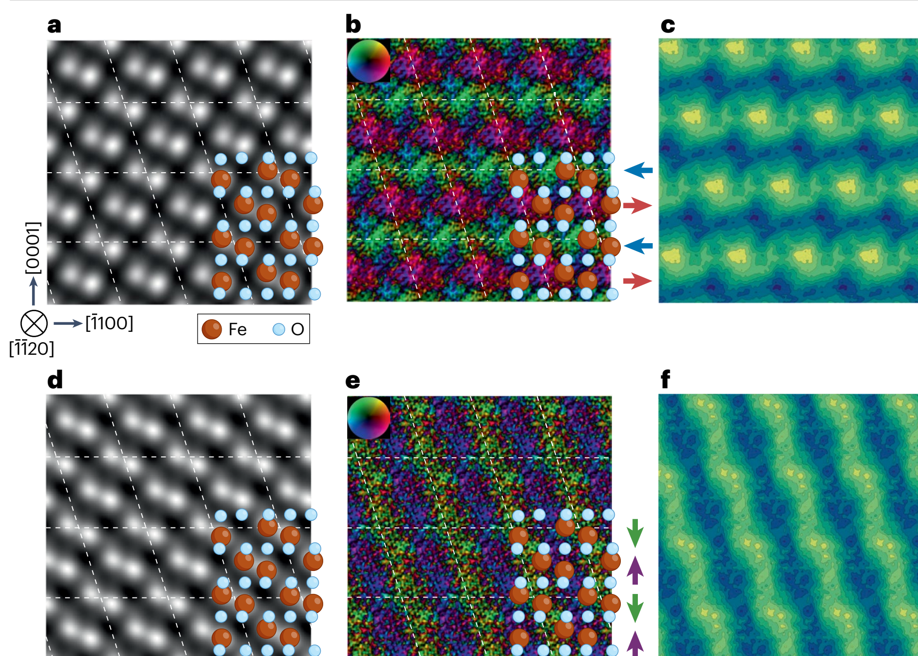

Fig. 7 | Atomic magnetic field imaging of antiferromagnetic α-Fe_2O_3. High-angle annular dark-field (HAADF) (panel **a**), differential phase-contrast (DPC) magnetic-field-vector colour map (panel **b**) and magnetic phase image (panel **c**) of α-Fe_2O_3 at room temperature. HAADF (panel **d**), DPC magnetic-field-vector colour map (panel **e**) and magnetic phase image (panel **f**) of α-Fe_2O_3 at 113 K. Structure models of α-Fe_2O_3 are superimposed in panels **a**, **b**, **d** and **e**. Schematics of spin direction at room temperature and at 113 K are shown in panels **b** and **e**, respectively. The same image filtering and unit cell averaging were applied in panels **b** and **e**. Scale bar in panel **a** corresponds to 0.5 nm. Adapted from ref. 81, Springer Nature Limited.

real materials and devices. We hope that the capabilities of advanced DPC STEM shown in this Review will contribute to the research and development of future electronic and spintronic devices.

However, there is still room for further developments in DPC STEM. We summarize such future directions for DPC STEM as follows.

Improvement in dose efficiency

Previous studies have discussed the issues of dose and signal-to-noise ratio in DPC STEM[162,163]. According to these results, to capture weaker electromagnetic fields with smaller electron probe size – that is, with higher spatial resolution – an increase in electron dose is essential. However, the high-dose imaging condition poses a problem of beam damage. Future developments in DPC STEM should focus on addressing this issue by developing imaging techniques with ultrahigh signal-to-noise ratio, by enhancing hardware performance (such as detector efficiency, fast scanning systems[164]), developing efficient image processing[91,97] and integrating machine learning approaches[165–167].

Upgrading image simulation techniques

For quantitative electromagnetic field analysis, especially in thick samples and/or imaging complex electromagnetic field structures, comparison between experimental images and image simulations is likely to be crucial. Developing advanced image simulation techniques, such as the recently proposed multislice algorithm with ab initio descriptions, must be further pursued[168,169].

Combining with in situ techniques

In situ or operando imaging techniques have been rapidly developed in the electron microscopy community[55,170–174]. It will be powerful to apply these in-situ techniques for electromagnetic field imaging of materials and devices under working conditions. To do this, fast beam scanning is essential. Recently, a fast beam-scan system for STEM has been developed[164]. Further improvements in scan speed and detector speed are likely to be indispensable for practical in situ DPC STEM imaging.

Disentangling electric and magnetic field information

When conducting DPC STEM observation from regions where an electric field and magnetic field coexist, the DPC STEM image reflects both contributions. Therefore, to extract pure magnetic field information, we need to separate the electric field signals, including the contribution of the mean inner potential changes, from the DPC image. Several separation methods have been proposed and applied in electron holography and DPC STEM[81,158,175–177]. However, these methods are not yet universally applicable or perfect, and thus we need to further explore the most suitable separation methods for DPC magnetic field imaging.

Published online: 26 November 2024

References

1. Morishita, S. et al. Attainment of 40.5 pm spatial resolution using 300 kV scanning transmission electron microscope equipped with fifth-order aberration corrector. *Microscopy* **67**, 46–50 (2018).
2. Haider, M., Braunshausen, G. & Schwan, E. Correction of the spherical aberration of a 200 kV TEM by means of a hexapole-corrector. *Optik* **99**, 167–179 (1995).
3. Haider, M. et al. Electron microscopy image enhanced. *Nature* **392**, 768–769 (1998).
4. Krivanek, O. L., Dellby, N. & Lupini, A. R. Towards sub-Å electron beams. *Ultramicroscopy* **78**, 1–11 (1999).
5. Batson, P. E., Dellby, N. & Krivanek, O. L. Sub-angstrom resolution using aberration corrected electron optics. *Nature* **418**, 617–620 (2002).
6. Pennycook, S. J. & Jesson, D. E. High-resolution incoherent imaging of crystals. *Phys. Rev. Lett.* **64**, 938–941 (1990).
7. Pennycook, S. J. & Jesson, D. E. High-resolution Z-contrast imaging of crystals. *Ultramicroscopy* **37**, 14–38 (1991).
8. Varela, M. et al. Materials characterization in the aberration-corrected scanning transmission electron microscope. *Annu. Rev. Mater. Res.* **35**, 539–569 (2005).
9. Findlay, S. D. et al. Direct imaging of hydrogen within a crystalline environment. *Appl. Phys. Express* **3**, 116603 (2010).
10. Ishikawa, R. et al. Direct imaging of hydrogen-atom columns in a crystal by annular bright-field electron microscopy. *Nat. Mater.* **10**, 278–281 (2011).
11. Findlay, S. D., Huang, R., Ishikawa, R., Shibata, N. & Ikuhara, Y. Direct visualization of lithium via annular bright field scanning transmission electron microscopy: a review. *Microscopy* **66**, 3–14 (2017).
12. Chu, M. W., Liou, S. C., Chang, C. P., Choa, F. S. & Chen, C. H. Emergent chemical mapping at atomic-column resolution by energy-dispersive X-ray spectroscopy in an aberration-corrected electron microscope. *Phys. Rev. Lett.* **104**, 196101 (2010).
13. Jeanguillaume, C. & Colliex, C. Spectrum-image: the next step in EELS digital acquisition and processing. *Ultramicroscopy* **28**, 252–257 (1989).
14. Hunt, J. A. & Williams, D. B. Electron energy-loss spectrum-imaging. *Ultramicroscopy* **38**, 47–73 (1991).
15. Shibata, N. et al. New area detector for atomic-resolution scanning transmission electron microscopy. *J. Electron Microsc.* **59**, 473–479 (2010).
16. Caswell, T. A. et al. A high-speed area detector for novel imaging techniques in a scanning transmission electron microscope. *Ultramicroscopy* **109**, 304–311 (2009).
17. Yang, H. et al. 4D STEM: high efficiency phase contrast imaging using a fast pixelated detector. *J. Phys. Conf. Ser.* https://doi.org/10.1088/1742-6596/644/1/012032 (2015).
18. Paterson, G. W. et al. Sub-100 nanosecond temporally resolved imaging with the Medipix3 direct electron detector. *Ultramicroscopy* **210**, 112917 (2019).
19. MacLaren, I., Macgregor, T. A., Allen, C. S. & Kirkland, A. I. Detectors — the ongoing revolution in scanning transmission electron microscopy and why this important to material characterization. *APL Mater.* **8**, 110901 (2020).
20. Tate, M. W. et al. High dynamic range pixel array detector for scanning transmission electron microscopy. *Microsc. Microanal.* **22**, 237–249 (2016).
21. Cao, M. C. et al. Theory and practice of electron diffraction from single atoms and extended objects using an EMPAD. *Microscopy* **67**, i150–i161 (2018).
22. Nord, M. et al. Fast pixelated detectors in scanning transmission electron microscopy. part I: data acquisition, live processing, and storage. *Microsc. Microanal.* **26**, 653–666 (2020).
23. Stroppa, D. G. et al. From STEM to 4D STEM: ultrafast diffraction mapping with a hybrid-pixel detector. *Microscopy Today* **31**, 10–14 (2023).
24. Zambon, P. et al. KITE: high frame rate, high count rate pixelated electron counting ASIC for 4D STEM applications featuring high-Z sensor. *Nucl. Instrum. Methods Phys. Res. A* **1048**, 167888 (2023).
25. Ophus, C. Quantitative scanning transmission electron microscopy for materials science: imaging, diffraction, spectroscopy, and tomography. *Annu. Rev. Mater. Res.* **53**, 105–141 (2023).
26. Paterson, G. W. et al. Fast pixelated detectors in scanning transmission electron microscopy. Part II: post-acquisition data processing, visualization, and structural characterization. *Microsc. Microanal.* **26**, 944–963 (2020).
27. Ooe, K., Seki, T., Ikuhara, Y. & Shibata, N. Ultra-high contrast STEM imaging for segmented/pixelated detectors by maximizing the signal-to-noise ratio. *Ultramicroscopy* **220**, 113133 (2021).
28. Ooe, K. et al. Direct imaging of local atomic structures in zeolite using optimum bright-field scanning transmission electron microscopy. *Sci. Adv.* **9**, eadf6865 (2023).
29. Jiang, Y. et al. Electron ptychography of 2D materials to deep sub-angstrom resolution. *Nature* **559**, 343–349 (2018).
30. Zhou, L. et al. Low-dose phase retrieval of biological specimens using cryo-electron ptychography. *Nat. Commun.* **11**, 2773 (2020).
31. Zhang, H. et al. Three-dimensional inhomogeneity of zeolite structure and composition revealed by electron ptychography. *Science* **380**, 633–638 (2023).
32. Rose, H. Phase contrast in scanning transmission electron microscopy. *Optik* **39**, 416–436 (1974).
33. Dekkers, D. H. & de Lang, H. Differential phase contrast in a STEM. *Optik* **41**, 452–456 (1974).
34. Rose, H. Nonstandard imaging methods in electron microscopy. *Ultramicroscopy* **2**, 251–267 (1976).
35. Chapman, J. N. The investigation of magnetic domain structures in thin foils by electron microscopy. *J. Phys. D: Appl. Phys.* **17**, 623–647 (1984).
36. Chapman, J. N., McFadyen, I. R. & McVitie, S. Modified differential phase contrast Lorentz microscopy for improved imaging of magnetic structures. *IEEE Trans. Magnetics* **26**, 1506–1511 (1990).
37. Shibata, N. et al. Imaging of built-in electric field at a p–n junction by scanning transmission electron microscopy. *Sci. Rep.* **5**, 10040 (2015).
38. Lohr, M. et al. Quantitative measurements of internal electric fields with differential phase contrast microscopy on InGaN/GaN quantum well structures. *Phys. Status Solidi* **253**, 140–144 (2016).
39. Carvalho, D. et al. Direct measurement of polarization-induced fields in GaN/AlN by nano-beam electron diffraction. *Sci. Rep.* **6**, 28459 (2016).
40. Brown, H. G. et al. Measuring nanometre-scale electric fields in scanning transmission electron microscopy using segmented detectors. *Ultramicroscopy* **182**, 169–178 (2017).
41. Nakamura, A., Kohno, Y., Sasaki, H. & Shibata, N. Differential phase contrast imaging with reduced dynamical diffraction effect. *Microsc. Microanal.* **23**, 1412–1413 (2017).

42. Haas, B., Rouviere, J. L., Boureau, V., Berthier, R. & Cooper, D. Direct comparison of off-axis holography and differential phase contrast for the mapping of electric fields in semiconductors by transmission electron microscopy. *Ultramicroscopy* **198**, 58–72 (2019).
43. Muller-Caspary, K. et al. Electrical polarization in AlN/GaN nanodisks measured by momentum-resolved 4D scanning transmission electron microscopy. *Phys. Rev. Lett.* **122**, 106102 (2019).
44. Bruas, L. et al. Improved measurement of electric fields by nanobeam precession electron diffraction. *J. Appl. Phys.* **127**, 205703 (2020).
45. Toyama, S. et al. Quantitative electric field mapping of a p–n junction by DPC STEM. *Ultramicroscopy* **216**, 113033 (2020).
46. Grieb, T. et al. 4D-STEM at interfaces to GaN: centre-of-mass approach & NBED-disc detection. *Ultramicroscopy* **228**, 113321 (2021).
47. da Silva, B. C. et al. Assessment of active dopants and p–n junction abruptness using in situ biased 4D-STEM. *Nano Lett.* **22**, 9544–9550 (2022).
48. Toyama, S. et al. Quantitative electric field mapping in semiconductor heterostructures via tilt-scan averaged DPC STEM. *Ultramicroscopy* **238**, 113538 (2022).
This article describes development of tDPC STEM by quantitative evaluation of residual diffraction contrast in semiconductor heterostructures, using both experiment and simulation.
49. Jia, Q. & Gloter, A. Real-space observation of potential reconstruction at metallic/insulating oxide interface. *Adv. Mater. Interfaces* https://doi.org/10.1002/admi.202202165 (2022).
50. Shibata, N. et al. Differential phase-contrast microscopy at atomic resolution. *Nat. Phys.* **8**, 611–615 (2012).
51. MacLaren, I. et al. On the origin of differential phase contrast at a locally charged and globally charge-compensated domain boundary in a polar-ordered material. *Ultramicroscopy* **154**, 57–63 (2015).
52. Taplin, D. J., Shibata, N., Weyland, M. & Findlay, S. D. Low magnification differential phase contrast imaging of electric fields in crystals with fine electron probes. *Ultramicroscopy* **169**, 69–79 (2016).
53. Campanini, M., Erni, R., Yang, C. H., Ramesh, R. & Rossell, M. D. Periodic giant polarization gradients in doped $BiFeO_3$ thin films. *Nano Lett.* **18**, 717–724 (2018).
54. Campanini, M. & et al. Atomic-resolution differential phase contrast STEM on ferroelectric materials: a mean-field approach. *Phys. Rev. B* https://doi.org/10.1103/PhysRevB.101.184116 (2020).
55. Huang, Q. et al. Direct observation of nanoscale dynamics of ferroelectric degradation. *Nat. Commun.* **12**, 2095 (2021).
56. Addiego, C. et al. Multiscale electric-field imaging of polarization vortex structures in $PbTiO_3$/$SrTiO_3$ superlattices.*APL Mater.* https://doi.org/10.1063/5.0146713 (2023).
57. Muller, K. et al. Atomic electric fields revealed by a quantum mechanical approach to electron picodiffraction. *Nat. Commun.* **5**, 5653 (2014).
58. Shibata, N. et al. Electric field imaging of single atoms. *Nat. Commun.* **8**, 15631 (2017).
59. Xu, J. et al. Atomic-level polarization in electric fields of defects for electrocatalysis. *Nat. Commun.* **14**, 7849 (2023).
60. Sanchez-Santolino, G. et al. Probing the internal atomic charge density distributions in real space. *ACS Nano* **12**, 8875–8881 (2018).
61. Ishikawa, R. et al. Direct electric field imaging of graphene defects. *Nat. Commun.* **9**, 3878 (2018).
62. Müller-Caspary, K. et al. Atomic-scale quantification of charge densities in two-dimensional materials. *Phys. Rev. B* https://doi.org/10.1103/PhysRevB.98.121408 (2018).
63. Fang, S. et al. Atomic electrostatic maps of 1D channels in 2D semiconductors using 4D scanning transmission electron microscopy. *Nat. Commun.* **10**, 1127 (2019).
64. Gao, W. et al. Real-space charge-density imaging with sub-angstrom resolution by four-dimensional electron microscopy. *Nature* **575**, 480–484 (2019).
65. Dyck, O. et al. Direct imaging of electron density with a scanning transmission electron microscope. *Nat. Commun.* **14**, 7550 (2023).
66. Zweck, J. Imaging of magnetic and electric fields by electron microscopy. *J. Phys. Condens. Matter* **28**, 403001 (2016).
67. Shibata, N. et al. Direct visualization of local electromagnetic field structures by scanning transmission electron microscopy. *Acc. Chem. Res.* **50**, 1502–1512 (2017).
68. Chen, C. et al. Direct determination of atomic structure and magnetic coupling of magnetite twin boundaries. *ACS Nano* **12**, 2662–2668 (2018).
69. Murakami, Y. O. et al. Magnetic-structure imaging in polycrystalline materials by specimen-tilt series averaged DPC STEM. *Microscopy* **69**, 312–320 (2020).
This article demonstrates the effect of sample-tilt-averaging DPC STEM for observing magnetic fields in a polycrystalline magnet.
70. Almeida, T. P. et al. Direct visualization of the magnetostructural phase transition in nanoscale FeRh thin films using differential phase contrast imaging. *Phys. Rev. Mater.* https://doi.org/10.1103/PhysRevMaterials.4.034410 (2020).
71. Hopkinson, D. G. et al. Nanometre imaging of Fe_3GeTe_2 ferromagnetic domain walls. *Nanotechnology* **32**, 205703 (2021).
72. Matsumoto, T. et al. Jointed magnetic skyrmion lattices at a small-angle grain boundary directly visualized by advanced electron microscopy. *Sci. Rep.* **6**, 35880 (2016).
73. Matsumoto, T. et al. Direct observation of Sigma7 domain boundary core structure in magnetic skyrmion lattice. *Sci. Adv.* **2**, e1501280 (2016).
74. Matsumoto, T., So, Y. G., Kohno, Y., Ikuhara, Y. & Shibata, N. Stable magnetic skyrmion states at room temperature confined to corrals of artificial surface pits fabricated by a focused electron beam. *Nano Lett.* **18**, 754–762 (2018).
75. Pollath, S. et al. Spin structure relation to phase contrast imaging of isolated magnetic Bloch and Neel skyrmions. *Ultramicroscopy* **212**, 112973 (2020).
76. Yasin, F. S. et al. Bloch lines constituting antiskyrmions captured via differential phase contrast. *Adv. Mater.* **32**, e2004206 (2020).
77. Kohno, Y., Nakamura, A., Morishita, S. & Shibata, N. Development of tilt-scan system for differential phase contrast scanning transmission electron microscopy. *Microscopy* **71**, 111–116 (2022).
This article describes the development of the tilt-scan hardware and system for tDPC STEM.
78. Shibata, N. et al. Atomic resolution electron microscopy in a magnetic field free environment. *Nat. Commun.* **10**, 2308 (2019).
This article develops and demonstrates magnetic-field-free atomic resolution STEM.
79. Toyama, S. et al. Real-space observation of a two-dimensional electron gas at semiconductor heterointerfaces. *Nat. Nanotechnol.* **18**, 521–528 (2023).
This article describes quantitative real-space observation of a 2D electron gas at semiconductor heterointerfaces using tDPC STEM.
80. Kohno, Y., Seki, T., Tsuruoka, S., Ohya, S. & Shibata, N. Magnetic field observation in a magnetic tunnel junction by scanning transmission electron microscopy. *Microscopy* https://doi.org/10.1093/jmicro/dfad063 (2023).
This article demonstrates magnetic field observation in a magnetic tunnel junction by tDPC STEM.
81. Kohno, Y., Seki, T., Findlay, S. D., Ikuhara, Y. & Shibata, N. Real-space visualization of intrinsic magnetic fields of an antiferromagnet. *Nature* **602**, 234–239 (2022).
This article demonstrates real-space visualization of atomic magnetic field inside antiferromagnetic haematite using magnetic-field-free atomic-resolution DPC STEM.
82. Waddell, E. M. C. J.N. Linear imaging of strong phase objects using asymmetrical detectors in STEM. *Optik* **54**, 83–96 (1979).
83. Chapman, J. N., Batson, P. E., Waddell, E. M. & Ferrier, R. P. The direct determination of magnetic domain wall profiles by differential phase contrast electron microscopy. *Ultramicroscopy* **3**, 203–214 (1978).
84. MacCallum, B. C., Landauer, M. N. & Rodenburg, J. M. Complex image reconstruction of weak specimens from a three-sector detector in the STEM. *Optik* **101**, 53–62 (1995).
85. Close, R., Chen, Z., Shibata, N. & Findlay, S. D. Towards quantitative, atomic-resolution reconstruction of the electrostatic potential via differential phase contrast using electrons. *Ultramicroscopy* **1591**, 124–137 (2015).
86. Majert, S. & Kohl, H. High-resolution STEM imaging with a quadrant detector-conditions for differential phase contrast microscopy in the weak phase object approximation. *Ultramicroscopy* **148**, 81–86 (2015).
87. Brown, H. G. et al. Structure retrieval with fast electrons using segmented detectors. *Phys. Rev. B* https://doi.org/10.1103/PhysRevB.93.134116 (2016).
88. Lazic, I., Bosch, E. G. T. & Lazar, S. Phase contrast STEM for thin samples: Integrated differential phase contrast. *Ultramicroscopy* **160**, 265–280 (2016).
89. Lopatin, S., Ivanov, Y. P., Kosel, J. & Chuvilin, A. Multiscale differential phase contrast analysis with a unitary detector. *Ultramicroscopy* **162**, 74–81 (2016).
90. Zweck, J., Schwarzhuber, F., Wild, J. & Galioit, V. On detector linearity and precision of beam shift detection for quantitative differential phase contrast applications. *Ultramicroscopy* **168**, 53–64 (2016).
91. Ishizuka, A., Oka, M., Seki, T., Shibata, N. & Ishizuka, K. Boundary-artifact-free determination of potential distribution from differential phase contrast signals. *Microscopy* **66**, 397–405 (2017).
92. Muller-Caspary, K. et al. Measurement of atomic electric fields and charge densities from average momentum transfers using scanning transmission electron microscopy. *Ultramicroscopy* **178**, 62–80 (2017).
93. Seki, T. et al. Quantitative electric field mapping in thin specimens using a segmented detector: revisiting the transfer function for differential phase contrast. *Ultramicroscopy* **182**, 258–263 (2017).
94. Yucelen, E., Lazic, I. & Bosch, E. G. T. Phase contrast scanning transmission electron microscopy imaging of light and heavy atoms at the limit of contrast and resolution. *Sci. Rep.* **8**, 2676 (2018).
95. Seki, T., Takanashi, N. & Abe, E. Integrated contrast-transfer-function for aberration-corrected phase-contrast STEM. *Ultramicroscopy* **194**, 193–198 (2018).
96. Seki, T. et al. Linear imaging theory for differential phase contrast and other phase imaging modes in scanning transmission electron microscopy. *Ultramicroscopy* **240**, 113580 (2022).
This article proposes linear imaging theory for DPC, detailing various imaging characteristics including defocus dependencies.
97. Zweck, J., Schwarzhuber, F., Pöllath, S. & Müller-Caspary, K. Advanced processing of differential phase contrast data: distinction between different causes of electron phase shifts. *Ultramicroscopy* https://doi.org/10.1016/j.ultramic.2023.113752 (2023).
98. Liang, Z., Song, D. & Ge, B. Optimizing experimental parameters of integrated differential phase contrast (iDPC) for atomic resolution imaging. *Ultramicroscopy* **246**, 113686 (2023).
99. Sakurai, J. J. & Napolitano, J. *Modern Quantum Mechanics* 3rd edn (2020).
100. Lippmann, B. A. Ehrenfest's theorem and scattering theory. *Phys. Rev. Lett.* **15**, 11–14 (1965).
101. Seki, T., Ikuhara, Y. & Shibata, N. Toward quantitative electromagnetic field imaging by differential-phase-contrast scanning transmission electron microscopy. *Microscopy* **70**, 148–160 (2021).

102. Iakoubovskii, K., Mitsuishi, K., Nakayama, Y. & Furuya, K. Thickness measurements with electron energy loss spectroscopy. *Microsc. Res. Tech.* **71**, 626–631 (2008).
103. Egerton, R. F. *Electron Energy-Loss Spectroscopy in the Electron Microscope* (Springer, 2011).
104. Allen, S. M. Foil thickness measurements from convergent-beam diffraction patterns. *Phil. Mag. A* **43**, 325–335 (2006).
105. Seki, T., Ikuhara, Y. & Shibata, N. Iterative algorithm of atomic potential reconstruction based on DPC signal from thick specimens. *Microsc. Microanal.* **25**, 60–61 (2019).
106. Addiego, C., Gao, W. & Pan, X. Thickness and defocus dependence of inter-atomic electric fields measured by scanning diffraction. *Ultramicroscopy* **208**, 112850 (2020).
107. Rose, H. Minimum-dose phase-contrast tomography by successive numerical optical sectioning employing the aberration-corrected STEM and a pixelated detector. *Ultramicroscopy* https://doi.org/10.1016/j.ultramic.2022.113484 (2022).
108. Mawson, T. et al. Suppressing dynamical diffraction artefacts in differential phase contrast scanning transmission electron microscopy of long-range electromagnetic fields via precession. *Ultramicroscopy* **219**, 113097 (2020).
109. Phatak, C., Petford-Long, A. K. & De Graef, M. Recent advances in Lorentz microscopy. *Curr. Opin. Solid. State Mater. Sci.* **20**, 107–114 (2016).
110. Krajnak, M., McGrouther, D., Maneuski, D., Shea, V. O. & McVitie, S. Pixelated detectors and improved efficiency for magnetic imaging in STEM differential phase contrast. *Ultramicroscopy* **165**, 42–50 (2016).
111. Wu, L., Han, M. G. & Zhu, Y. Toward accurate measurement of electromagnetic field by retrieving and refining the center position of non-uniform diffraction disks in Lorentz 4D-STEM. *Ultramicroscopy* **250**, 113745 (2023).
112. Wang, B., Bagues, N., Liu, T., Kawakami, R. K. & McComb, D. W. Extracting weak magnetic contrast from complex background contrast in plan-view FeGe thin films. *Ultramicroscopy* **232**, 113395 (2022).
113. Tsuda, K. & Tanaka, M. Refinement of crystal structural parameters using two-dimensional energy-filtered CBED patterns. *Acta Crystallogr. A* **55**, 939–954 (1999).
114. Chapman, J. N. & Scheinfein, M. R. Transmission electron microscopies of magnetic microstructures. *J. Magn. Magn. Mater.* **200**, 729–740 (1999).
115. Tsuno, K. T. T. Ferro-megnetic material observatio lens system for CTEM with a eucentric goniometer. *J. Electron. Microsc.* https://doi.org/10.1093/oxfordjournals.jmicro.a050032 (1976).
116. Shindo, D. et al. Electron holography of Nd–Fe–B nanocomposite magnets. *Scr. Mater.* **48**, 851–856 (2003).
117. Chen, Z. et al. Lorentz electron ptychography for imaging magnetic textures beyond the diffraction limit. *Nat. Nanotechnol.* **17**, 1165–1170 (2022).
118. Kohno, Y., Morishita, S. & Shibata, N. New STEM/TEM objective lens for atomic resolution lorentz imaging. *Microsc. Microanal.* **23**, 456–457 (2017).
119. Seki, T. et al. Incommensurate grain-boundary atomic structure. *Nat. Commun.* **14**, 7806 (2023).
This article reveals the unique atomic structure of an Fe–3%Si grain boundary via magnetic-field-free atomic resolution STEM.
120. Ambacher, O. et al. Two-dimensional electron gases induced by spontaneous and piezoelectric polarization charges in N- and Ga-face AlGaN/GaN heterostructures. *J. Appl. Phys.* **85**, 3222–3233 (1999).
121. Ambacher, O. et al. Two dimensional electron gases induced by spontaneous and piezoelectric polarization in undoped and doped AlGaN/GaN heterostructures. *J. Appl. Phys.* **87**, 334–344 (2000).
122. Ohta, H. et al. Giant thermoelectric Seebeck coefficient of a two-dimensional electron gas in $SrTiO_3$. *Nat. Mater.* **6**, 129–134 (2007).
123. Smorchkova, I. P. et al. Polarization-induced charge and electron mobility in AlGaN/GaN heterostructures grown by plasma-assisted molecular-beam epitaxy. *J. Appl. Phys.* **86**, 4520–4526 (1999).
124. Ibbetson, J. P. et al. Polarization effects, surface states, and the source of electrons in AlGaN/GaN heterostructure field effect transistors. *Appl. Phys. Lett.* **77**, 250–252 (2000).
125. Zheng, Z. et al. Gallium nitride-based complementary logic integrated circuits. *Nat. Electron.* **4**, 595–603 (2021).
126. Pearton, S. J., Zolper, J. C., Shul, R. J. & Ren, F. GaN: processing, defects, and devices. *J. Appl. Phys.* **86**, 1–78 (1999).
127. Pearton, S. J. et al. Review of radiation damage in GaN-based materials and devices. *J. Vacuum Sci. Technol. A* https://doi.org/10.1116/1.4799504 (2013).
128. Joh, J. & del Alamo, J. A. A current-transient methodology for trap analysis for GaN high electron mobility transistors. *IEEE Trans. Electron. Devices* **58**, 132–140 (2011).
129. Nakagami, K., Ohno, Y., Kishimoto, S., Maezawa, K. & Mizutani, T. Surface potential measurements of AlGaN/GaN high-electron-mobility transistors by Kelvin probe force microscopy. *Appl. Phys. Lett.* **85**, 6028–6029 (2004).
130. Masuda, H., Ishida, N., Ogata, Y., Ito, D. & Fujita, D. Internal potential mapping of charged solid-state-lithium ion batteries using in situ Kelvin probe force microscopy. *Nanoscale* **9**, 893–898 (2017).
131. Cao, Y., Pomeroy, J. W., Uren, M. J., Yang, F. & Kuball, M. Electric field mapping of wide-bandgap semiconductor devices at a submicrometre resolution. *Nat. Electron.* **4**, 478–485 (2021).
132. Birner, S. et al. nextnano: general purpose 3-D simulations. *IEEE Trans. Electron. Devices* **54**, 2137–2142 (2007).
133. Ando, T. Self-consistent results for a $GaAs/Al_xGa_{1-x}As$ heterojunction. II. Low temperature mobility. *J. Phys. Soc. Jpn* **51**, 3900–3907 (1982).
134. Ando, T., Fowler, A. B. & Stern, F. Electronic properties of two-dimensional systems. *Rev. Mod. Phys.* **54**, 437–672 (1982).
135. Quang, D. N., Tuoc, V. N., Tung, N. H., Minh, N. V. & Phong, P. N. Roughness-induced mechanisms for electron scattering in wurtzite group-III-nitride heterostructures. *Phys. Rev. B* https://doi.org/10.1103/PhysRevB.72.245303 (2005).
136. Quang, D. N. et al. Quantum and transport lifetimes due to roughness-induced scattering of a two-dimensional electron gas in wurtzite group-III-nitride heterostructures. *Phys. Rev. B* https://doi.org/10.1103/PhysRevB.74.205312 (2006).
137. Butté, R. et al. Current status of AlInN layers lattice-matched to GaN for photonics and electronics. *J. Phys. D* **40**, 6328–6344 (2007).
138. Crespo, A. et al. High-power Ka-band performance of AlInN/GaN HEMT with 9.8-nm-thin barrier. *IEEE Electron. Device Lett.* **31**, 2–4 (2010).
139. Py, M. A., Lugani, L., Taniyasu, Y., Carlin, J.-F. & Grandjean, N. Shallow donor and deep DX-like center in InAlN layers nearly lattice-matched to GaN. *Phys. Rev. B* https://doi.org/10.1103/PhysRevB.90.115208 (2014).
140. Kappers, M. J., Zhu, T., Sahonta, S. L., Humphreys, C. J. & Oliver, R. A. SCM and SIMS investigations of unintentional doping in III-nitrides. *Phys. Status Solidi C.* **12**, 403–407 (2015).
141. Gutfleisch, O. et al. Magnetic materials and devices for the 21st century: stronger, lighter, and more energy efficient. *Adv. Mater.* **23**, 821–842 (2011).
142. Sagawa, M., Hirosawa, S., Yamamoto, H., Fujimura, S. & Matsuura, Y. Nd–Fe–B permanent magnet materials. *Jpn. J. Appl. Phys*. https://doi.org/10.1143/jjap.26.785 (1987).
143. Gutfleisch, O. Controlling the properties of high energy density permanent magnetic materials by different processing routes. *J. Phys. D* **33**, R157–R172 (2000).
144. Harland, C. L. & Davies, H. A. Magnetic properties of melt-spun Nd-rich NdFeB alloys with Dy and Ga substitutions. *J. Alloy. Compd.* **281**, 37–40 (1998).
145. Sepehri-Amin, H., Ohkubo, T. & Hono, K. The mechanism of coercivity enhancement by the grain boundary diffusion process of Nd–Fe–B sintered magnets. *Acta Materialia* **61**, 1982–1990 (2013).
146. Sagawa, M., Fujimura, S., Togawa, N., Yamamoto, H. & Matsuura, Y. New material for permanent magnets on a base of Nd and Fe (invited). *J. Appl. Phys.* **55**, 2083–2087 (1984).
147. Croat, J. J., Herbst, J. F., Lee, R. W. & Pinkerton, F. E. Pr–Fe and Nd–Fe-based materials: a new class of high-performance permanent magnets (invited). *J. Appl. Phys.* **55**, 2078–2082 (1984).
148. Zhu, J.-G., Zheng, Y. & Prinz, G. A. Ultrahigh density vertical magnetoresistive random access memory (invited). *J. Appl. Phys.* **87**, 6668–6673 (2000).
149. Bhatti, S. et al. Spintronics based random access memory: a review. *Mater. Today* **20**, 530–548 (2017).
150. Julliere, M. Tunneling between ferromagnetic films. *Phys. Lett. A* **54**, 225–226 (1975).
151. Miyazaki, T. & Tezuka, N. Giant magnetic tunneling effect in $Fe/Al_2O_3/Fe$ junction. *J. Magn. Magn. Mater.* **139**, L231–L234 (1995).
152. Moodera, J. S., Kinder, L. R., Wong, T. M. & Meservey, R. Large magnetoresistance at room temperature in ferromagnetic thin film tunnel junctions. *Phys. Rev. Lett.* **74**, 3273–3276 (1995).
153. Parkin, S. S. et al. Giant tunnelling magnetoresistance at room temperature with MgO (100) tunnel barriers. *Nat. Mater.* **3**, 862–867 (2004).
154. Yuasa, S., Nagahama, T., Fukushima, A., Suzuki, Y. & Ando, K. Giant room-temperature magnetoresistance in single-crystal Fe/MgO/Fe magnetic tunnel junctions. *Nat. Mater.* **3**, 868–871 (2004).
155. Rother, A. & Scheerschmidt, K. Relativistic effects in elastic scattering of electrons in TEM. *Ultramicroscopy* **109**, 154–160 (2009).
156. Edstrom, A., Lubk, A. & Rusz, J. Quantum mechanical treatment of atomic-resolution differential phase contrast imaging of magnetic materials. *Phys. Rev. B* https://doi.org/10.1103/PhysRevB.99.174428 (2019).
157. Tanigaki, T. et al. Electron holography observation of individual ferrimagnetic lattice planes. *Nature* **631**, 521–525 (2024).
158. Tanigaki, T. et al. Magnetic field observations in CoFeB/Ta layers with 0.67-nm resolution by electron holography. *Sci. Rep.* **7**, 16598 (2017).
159. Shull, C. G., Strauser, W. A. & Wollan, E. O. Neutron diffraction by paramagnetic and antiferromagnetic substances. *Phys. Rev.* **83**, 333–345 (1951).
160. Brok, E. et al. Spin orientation in solid solution hematite-ilmenite. *Am. Mineralogist* **102**, 1234–1243 (2017).
161. Morin, F. J. Magnetic susceptibility of αFe_2O_3 and αFe_2O_3 with added titanium. *Phys. Rev.* **78**, 819–820 (1950).
162. Pollath, S., Schwarzhuber, F. & Zweck, J. The differential phase contrast uncertainty relation: connection between electron dose and field resolution. *Ultramicroscopy* **228**, 113342 (2021).
163. Seki, T., Ikuhara, Y. & Shibata, N. Theoretical framework of statistical noise in scanning transmission electron microscopy. *Ultramicroscopy* **193**, 118–125 (2018).
164. Kusumi, T. et al. Fast reconstruction of scanning transmission electron microscopy images using Markov random field model. *Ultramicroscopy* **253**, 113811 (2023).
165. Kalinin, S. V. et al. Machine learning in scanning transmission electron microscopy. *Nat. Rev. Methods Primers* https://doi.org/10.1038/s43586-022-00095-w (2022).
166. Ziatdinov, M., Ghosh, A., Wong, C. Y. & Kalinin, S. V. AtomAI framework for deep learning analysis of image and spectroscopy data in electron and scanning probe microscopy. *Nat. Mach. Intell*. https://doi.org/10.1038/s42256-022-00555-8 (2022).
167. Shi, C. et al. Uncovering material deformations via machine learning combined with four-dimensional scanning transmission electron microscopy. *npj Comput. Mater*. https://doi.org/10.1038/s41524-022-00793-9 (2022).

168. Madsen, J., Pennycook, T. J. & Susi, T. Ab initio description of bonding for transmission electron microscopy. *Ultramicroscopy* **231**, 113253 (2021).
169. Susi, T. et al. Efficient first principles simulation of electron scattering factors for transmission electron microscopy. *Ultramicroscopy* **197**, 16–22 (2019).
170. Anada, S. et al. Precise measurement of electric potential, field, and charge density profiles across a biased GaAs p–n tunnel junction by in situ phase-shifting electron holography. *J. Appl. Phys*. https://doi.org/10.1063/1.5006837 (2017).
171. Wang, L. et al. In-situ visualization of the space-charge-layer effect on interfacial lithium-ion transport in all-solid-state batteries. *Nat. Commun.* **11**, 5889 (2020).
172. Gatel, C. et al. Extended charge layers in metal-oxide-semiconductor nanocapacitors revealed by operando electron holography. *Phys. Rev. Lett.* **129**, 137701 (2022).
173. Yamashita, S. et al. Atomic-scale dynamics at solid–liquid nanointerfaces induced by electron-beam irradiation. *Nano Lett.* **22**, 10073–10079 (2022).
174. Yasin, F. S. et al. Real-space determination of the isolated magnetic skyrmion deformation under electric current flow. *Proc. Natl Acad. Sci. USA* **119**, e2200958119 (2022).
175. Tonomura, A. Electron-holographic interference microscopy. *Adv. Phys.* **41**, 59–103 (1992).
176. Campanini, M., Nasi, L., Albertini, F. & Erni, R. Disentangling nanoscale electric and magnetic fields by time-reversal operation in differential phase-contrast STEM. *Appl. Phys. Lett*. https://doi.org/10.1063/5.0026121 (2020).
177. Tonomura, A., Matsuda, T., Endo, J., Arii, T. & Mihama, K. Direct observation of fine structure of magnetic domain walls by electron holography. *Phys. Rev. Lett.* **44**, 1430–1433 (1980).
178. Peters, J. J. P. et al. Event-responsive scanning transmission electron microscopy. *Science* **385**, 549–553 (2024).
179. Jannis, D. et al. Event driven 4D STEM acquisition with a Timepix3 detector: microsecond dwell time and faster scans for high precision and low dose applications. *Ultramicroscopy* **233**, 113423 (2022).
180. Kuttruff, J., Holder, J., Meng, Y. & Baum, P. Real-time electron clustering in an event-driven hybrid pixel detector. *Ultramicroscopy* **255**, 113864 (2024).
181. Aso, R. et al. Direct identification of the charge state in a single platinum nanoparticle on titanium oxide. *Science* **378**, 202–206 (2022).
182. Song, K. et al. Direct imaging of the electron liquid at oxide interfaces. *Nat. Nanotechnol.* **13**, 198–203 (2018).
183. Zheng, F. et al. Hopfion rings in a cubic chiral magnet. *Nature* **623**, 718–723 (2023).

Acknowledgements

The authors thank S. Ohya for fabricating the model tunnel magnetoresistance device, Y. Kanitani, Y. Kudo and S. Tomiya for providing GaN heterostructure samples, H. Sasaki for providing the GaAs p–n junction sample, and A. Kinoshita and T. Shoji for providing the Nd–Fe–B polycrystalline magnet sample. This work was supported by JST ERATO grant number JPMJER2202, Japan. A part of this work was supported by JSPS KAKENHI grant numbers JP20H05659, JP19H05788, JP20K15014 and 22H04960. T.S. acknowledges support from JST-PRESTO grant number JPMJPR21AA. A part of this work was supported by the Advanced Research Infrastructure for Materials and Nanotechnology (ARIM) grant number JPMXP1222UT0044, sponsored by the Ministry of Education, Culture, Sports, Science and Technology (MEXT), Japan.

Author contributions

S.T. and N.S. contributed to researching data, discussion, writing and editing for the Review. T.S. and Y.K. contributed to discussion of content and reviewing of the manuscript. Y.I. contributed to discussion of content. Y.O.M. researched data for the Review.

Competing interests

The authors declare no competing interests.

Additional information

Peer review information *Nature Reviews Electrical Engineering* thanks Wolfgang Jäger, Xiaoxu Zhao and the other, anonymous, reviewer(s) for their contribution to the peer review of this work.

Publisher's note Springer Nature remains neutral with regard to jurisdictional claims in published maps and institutional affiliations.

Springer Nature or its licensor (e.g. a society or other partner) holds exclusive rights to this article under a publishing agreement with the author(s) or other rightsholder(s); author self-archiving of the accepted manuscript version of this article is solely governed by the terms of such publishing agreement and applicable law.

© Springer Nature Limited 2024